

Supplementary information for: Movement is governed by rotational population dynamics in spinal motor networks

1. INTRODUCTION

In this supplementary information, we describe the experimental protocols and supplementary results, and then the details of the theory and results from implementing the theory into models and simulations.

2. METHODS AND MATERIALS

A. Experimental methods

The surgical procedures comply with Danish legislation and were approved by the controlling body under the Ministry of Justice. The experimental data used in this study has been used in a previous publication for a different purpose [1]. Methods have previously been published in details in [2, 3]. Briefly described and adapted from previous publications [2, 4], 80 adult red-eared turtles (*Trachemys scripta elegans*) of both sexes were used in this study. The animal was placed on crushed ice for 2h. to ensure hypothermic anesthesia [3], then killed by decapitation and blood substituted by perfusion with a Ringer solution containing (in mM): 120 NaCl; 5 KCl; 15 NaHCO₃; 2MgCl₂; 3CaCl₂; and 20 glucose, saturated with 98% O₂ and 2% CO₂ to obtain pH 7.6. The carapace containing the D4-S2 spinal cord segments (corresponding to the cervical to lumbar regions) was isolated by transverse cuts and the cord was perfused with Ringer's solution through the vertebral foramen, via a steel tube and silicone gasket pressing against the D4 vertebra. The motor nerves was cut to measure their activity and increase mechanical by preventing movements of the limbs. The preparation was placed and glued on the back in a chamber with constant flow of oxygenated Ringer's solution to keep the cord submerged and the skin tissue moist [3]. The vertebrae (D8-D10) corresponding to the lumbar segments L2-L5 in mammals [5]. was carefully opened on the ventral side to allow access to spinal cord for insertion of the multi-electrode arrays.

B. Electrophysiology

For monitoring the rhythmic activity and motor program state, electroneurogram recordings (ENG) were performed with suction electrodes of the hip flexor, knee extensor nerves and the dD8-nerve [6], i.e. a total of six motor nerves (3 from each side) at the level of D9-D10 vertebra. The ENGs were recorded with a differential amplifier Iso-DAM8. The bandwidth was 300Hz–1kHz. Custom-designed Silicon probes (Berg64-probe with 15 μ m thickness, from Neuronexus inc.) was inserted into the lumbar spinal cord (D8, D9 and D10) in the anterior-posterior direction to minimize damage to the white matter fiber tracks. These segments correspond to the lumbar spinal cord in mammals [5]. A 256-channel recordings system (KJE-1001, Amplipex ltd, Szeged, Hungary) was used to acquire the extracellular potentials of a large number of neurons, for post-hoc polytrode spike sorting.

C. Motor network activation by cutaneous sensory input

Each scratch episode lasted approximately 20 s. A new trial was initiated after a 5 min rest. To reproducibly activate the scratching motor pattern, a linear actuator was applied to provide mechanical touch on the skin around the legs meeting the carapace. The somatic touch was controlled by a function generator (TT2000, Thurlby Thandar instrument, UK) and consisted of a ten-second long sinusoidal movement (1-2 Hz). The touch was applied on the border of the carapace marginal shields M9-M10 and the soft tissue surrounding the hind limb, which is the receptive field for inducing pocket scratching motor pattern. Pocket scratching was elicited on

either right or left side on the soft tissue surrounding the hind limb representing two distinct behaviors. Further, rostral scratching behavior was elicited by similar touching of the carapace in the more rostral location on the shields. For reviews on the various motor patterns and the cutaneous activation see [7, 8].

D. Data analysis

All data analysis was performed in custom designed procedures either in Matlab (Mathworks, R2020b) or Python (www.python.org). Spike sorting was performed using KlustaKwik [9]. Spike rates were estimated by convolving the neuronal spike times with a Gaussian kernel,

$$k(t) = \frac{1}{\sqrt{2\pi}\sigma} \exp\left(-\frac{t^2}{2\sigma^2}\right) \quad (S1)$$

where $\sigma = 250$ ms, to capture the slow firing rate modulation. The firing rates were further high-pass filtered with a 3-pole Butterworth filter using a zero-phase filter ('filtfilt.m') function in Matlab, with a cut-off frequency of 0.3 Hz. To better compare phase of neuronal activity, the firing rate amplitude was normalized to unity and the mean subtracted. To remove slow components, the firing rates and nerve traces was digitally filtered using a 3-pole Butterworth filter in both directions to cancel phase distortion. The fast activity was high pass filtered with cut off 5 Hz after removing any potential action potentials. The slow activity was band-pass filtered from 0.2–5Hz.

Principal component analysis (PCA) of the multidimensional population firing rates was performed on the firing rate space (neural space). The principal components U_n were determined as eigenvectors of the empirical covariance matrix C of the n firing rate traces, with the eigenvalues λ_n representing the proportion of variance in the data in that each component can account for. The eigenvectors and eigenvalues were found via:

$$CU = U\Sigma \quad (S2)$$

where $U = [U_1 U_2 \dots U_n]$ contains the principal components (eigenvectors) U_n and

$$\Sigma = \begin{bmatrix} \lambda_1 & 0 & \dots \\ \vdots & \ddots & \\ 0 & & \lambda_n \end{bmatrix} \quad (S3)$$

The PCA was performed in matlab using the function 'PCA.m'. Similar PC analysis was performed on the nerve activity, although this was only 6-dimensional data (Fig. 1).

Sorting of units according motor phase The firing rate of units was sorted according motor phase by two steps. First, the frequency of rhythmic activity was identified by estimating the peak in the power spectrum of a representative nerve. For this purpose, the nerve activity was rectified and smoothed and sub-sampled to have same sampling rate as the estimated firing rates. Second, the magnitude and phase of the coherence Coh_i between this nerve activity and the firing rate of the i th neuron was estimated via [10]:

$$Coh_i(f) = \frac{\sum_{j=1}^k R_{ij}(f) N_j(f)}{k \sqrt{S_{xxi} S_{nerve}}} \quad (S4)$$

where k is the number of multi-taper spectral estimates ($k = 4$). R_{ij} and N_j are the individual taper spectral estimates using discrete Fourier transform of the firing rate of the i th neuron, $r_i(t)$, and the rectified and low-pass filtered nerve trace $n(t)$:

$$R_{ij}(f) = \sum_{t=0}^T e^{j2\pi ft} r_i(t) w_j(t)$$

$$N_j(f) = \sum_{t=0}^T e^{j2\pi ft} n(t) w_j(t)$$

and $w_j(t)$ is the j th taper function, the discrete prolate spheroidal (Slepian) sequences [11]. These taper functions and the Fourier transforms were calculated using the matlab function 'dpss.m'

and 'fft.m'. The power spectra of the firing rate of the i th neuron and the nerve were calculated as $S_{xxi} = \frac{1}{k} \sum_{j=1}^{j=k} R_{ij} R_{ij}^*$ and $S_{nerve} = \frac{1}{k} \sum_{j=1}^{j=k} N_j N_j^*$, where the $*$ indicate complex conjugate. The phase of the i th neuron was chosen from $Coh_i(f)$ at the frequency where the strongest peak in S_{nerve} was found, which was the rhythm of the motor pattern. Based on the phase, the neurons was sorted and plotted (e.g. Fig. 1D-E).

Significance level could be assessed in coherence if the magnitude of coherence exceeded the following:

$$Coh > \sqrt{1 - p^{1/(nk-1)}} \quad (S5)$$

where p indicates the level of confidence. We used 95%-confidence, i.e. $p = 0.05$. The degrees of freedom is k , and since we used $k = 4$ tapers for spectral estimation, the confidence limit was at 0.79. The standard deviation was calculated using circular statistics as originally defined in [12] (section 2.3.3):

$$\sigma_{circular} = \sqrt{-2 \log(\bar{R})} \quad (S6)$$

i.e. involving the natural logarithm of \bar{R} is the mean resultant length of all observations in polar coordinates, hence \bar{R} is between 0 and 1. If the observations angles are close to each other the resultant length is close to 1 and the $\sigma_{circular}$ is close to 0.

Nerve activity measures In some of the analysis the motor output was measured as electroneurograms (ENGs) quantified using root mean square (RMS) of the traces after smoothing using the Savitzky-Golay finite impulse response filter. The RMS is the square root of the mean of the squared ENGs:

$$ENG_{RMS} = \sqrt{\frac{1}{n} (x_1^2 + x_2^2 + \dots + x_n^2)} \quad (S7)$$

where x_1, x_2, \dots, x_n are the ENG measurements and n is the number of samples. The RMS values were calculated in matlab using the procedure 'rms.m'. The mean values reported (Fig. 2) are the average of all 6 nerves. The error bars are the standard error of the means, i.e. the standard deviation divided by $\sqrt{6}$. A pairwise statistical comparison was performed between trials each having 6 measurements (the nerves) using the non-parametric Wilcoxon signed rank test via the procedure 'singrank.m' in matlab.

The relationship between radius of PC rotation (RMS of first two components) and nerve output (RMS) was verified using an F-statistic vs. constant model. Test statistic for the F-test on the regression model (Fig. S5G-H), is a tests of whether the linear fit is significantly better than only a constant term.

E. Network model: balanced sequence generator

The model consists of a network of interneurons and two or more nerve-readouts that represents the motor commands resulting from the network activity.

Interneuron network

The interneuron network consists of $N = 200$ neurons out of which half are excitatory and half are inhibitory. We model the activity of an example neuron i as a firing rate $\phi[g_i(t), x_i(t)]$ that depends on an activity variable $x_i(t)$, analogous to a membrane potential, and gain variable $g_i(t)$. We use a similar function to the one used in ([13]):

$$\phi(g_i, x_i) = \begin{cases} x_* (1 - \tanh[g(x - x_*)/x_*]), & \text{for } x \leq x_* \\ x_* + x_{\max} \tanh[g(x - x_*)/x_{\max}], & \text{for } x > x_* \end{cases} \quad (S8)$$

where x_* represents the input level at which the slope of the firing rate function has its maximum (resulting in an output firing rate of $\phi = x_*$ Hz) and x_{\max} is the maximum deviation (in terms of firing rates) from x_* . Here, we set $x_* = 20$ and $x_{\max} = 50$, resulting in a maximum firing rates of 70 Hz. The dynamics of the network is then determined by the equation

$$\tau \dot{x}_i(t) = -x_i(t) + \sum_j W_{ij} \phi[g_j(t), x_j(t)] + I_e(t) \quad (S9)$$

where $\tau = 50$ ms is a time constant representing the combined membrane and synaptic timescale, W is a matrix that describes the network connectivity (see below), and $I_e(t)$ is a time-varying external drive that consists of a constant input and a noise term $I_e(t) = I(t) + \epsilon$, where the noise term ϵ is Gaussian noise with zero mean and standard deviation $\sigma = 4$.

Network connectivity

The connectivity of the network is assumed to be sparse (as indicated by e.g. [4]) with a pair-wise connection probability $C = 0.1$. Excitatory (positive) weights J_{ex} are assumed to be equal in magnitude to inhibitory (negative) ones J_{in} . To ensure that the incoming connections are balanced for each neuron we construct the connectivity matrix in the following way: We start with a matrix in which all elements are zero. For each neuron we then select $CN/2$ presynaptic excitatory neurons and assigned them the weight J_{ex} and $CN/2$ presynaptic inhibitory neuron and assigned them the weight J_{in} . In this way we ensure that the network is both globally and locally balanced, i.e. the incoming synaptic weights are balanced for each neuron. The synaptic weight is set so that the connectivity matrix W has a spectral radius such that the largest eigenvalue $\lambda_{max}=1$ (on average over realizations), by setting

$$J_{ex} = \frac{1}{\sqrt{NC(1-C)}} \quad (S10)$$

and $J_{in} = -J_{ex}$ [14]. This results in a network that is on the edge of instability for a uniform gain $g=1$. As a default, we set $g=1.2$ which results in a linearly unstable network. For this study we selected connectivity matrices for which the largest eigenvalue λ_{max} had a non-zero imaginary part since these networks can be expected to generate oscillatory activity (see Mathematical note below).

Gain modulation for amplitude control

To control the amplitude of oscillations in the network model we adjusted the gain parameter g uniformly for all neurons in the network.

Gain modulation for frequency control: "Speed-" and "brake" cells

To control the frequency of oscillations in the network we adjusted the gain g_i individually for selected neurons in the network. A simple procedure was set up to estimate the influence of each neuron on the overall frequency: The gain g_i was increased and decreased by a small amount and the spectrum of the connectivity matrix W was calculated. Depending on whether that imaginary part of the largest eigenvalue λ_{max} was increased or decreased (corresponding to an expected increased or decreased oscillation frequency) we assigned the neuron an index dubbed the frequency "modulation capacity". A positive modulation capacity means that an increase in gain or drive to that neuron will increase the frequency of the rhythm, and vice versa for a negative modulation index. Since a detailed gain modulation of all neurons in the network can be considered less biologically plausible, we selected the 10% of neurons with the largest positive effect on the imaginary part and labelled them as 'speed' cells, and the 10% with the largest negative effect and labelled them 'brake' cells. To increase the network oscillation frequency we increased the gain of the 'speed' cells and decreased the gain of the 'brake' cells (Fig. 3). To decrease the network oscillation frequency we did the opposite, i.e. we decreased the gain of the 'speed' cells and increased the gain of the 'brake' cells.

Gain modulation for multi-functional activity: "Switch" cells

To generate different motor behaviour from the network we identified a subset of neurons that had a large influence on the phase distribution of the dominant eigenmode. Starting with a default value for the gain of $g = 1.1$ we first calculated the phase for each interneuron from the eigenvector corresponding to the largest eigenvalue of the connectivity matrix gW . We then increased the gain g_i of each neuron i individually and calculated the effect of the changed gain on the phase distribution of the resulting effective connectivity. The top 10% of the neurons that caused the largest change in the overall phase distribution (calculated as the circular standard deviation of the change in phase) were selected as 'switch' neurons. To generate two different distinct behaviours (see below) we set the gain of the 'switch' neurons to two different vectors with values between $g_i = 1.1 \pm 0.3$.

Nerve readout

The nerve activity was modeled using a Gaussian noise with zero mean and where the width (standard deviation) $\sigma(t)$ of the distribution depends on a threshold-linear readout from the interneuron network:

$$\sigma(t) = [\sum_i M_i \phi_i(t)]_+ \quad (S11)$$

where M_i represents the readout weights and $[]_+$ indicates that the width can only be positive. The readout weights were constrained to respect Dale's law, i.e. excitatory interneurons could only have a positive weights and inhibitory interneurons could only have negative weights. We used two different ways of setting up the linear readout:

Readout based on phase of dominant eigenmode The simplest method used was to set up to readout-weights M_i based on the phase of each neuron i in the network oscillation. The phase of all neurons was estimated from the eigenvector corresponding to the largest eigenvalue λ_{max} of the connectivity matrix W . To set up the readout for a specific nerve, we first assigned the nerve a phase θ_{nerve} . For excitatory neurons that had a phase of $\theta_{nerve} \pm \pi/8$ we set $M_i = 1$ and set $M_i = 0$ for all other excitatory neurons. To generate reciprocal inhibition in the nerve input, we selected inhibitory neuron with a phase of $(\theta_{nerve} + \pi) \pm \pi/8$ and set $M_i = -1$, while $M_i = 0$ for all other. To set up a pair of flexor-extensor nerves with alternating activity, we set $\theta_{flexor} = \pi/2$ and $\theta_{extensor} = -\pi/2$.

Optimized readout for multi-functional output We first selected two distinct gain vectors for pocket and rostral scratch, respectively (see above) and simulated network activity using these gain vectors. To find the appropriate read-out weights, we then set up target functions for each behaviour for the flexor- and extensor nerves that were phase-shifted by π . The pocket and rostral scratch behaviours had different relative timing between the knee- and hip flexor nerves, shifted by π as well as different amplitudes (Fig 4). Read-out weights were then found using a linear least-square algorithm with bounds on the variables such that the weights M_i could only be positive for excitatory neurons and negative for inhibitory neurons.

Limb movement model To translate the nerve readout to position of knee and foot we set up a simple model that integrates the nerve drive to calculate the angle Θ of the foot/knee resulting from the flexor and extensor nerves (Fig4):

$$\tau_{muscle}\dot{\Theta}(t) = w_{\Theta}[flexor(t) - extensor(t) - (\Theta - \Theta_0)] \quad (S12)$$

where $\tau_{muscle}=10$ ms represent the time scale with which a muscle responds to a nerve drive and w_{Θ} is a weight that give the force resulting from a specific drive. The last term on the right-hand side represents a weak decay back to the initial position of the limb.

3. SUPPLEMENTARY RESULTS

Five experimental data sets that fulfilled the requirements of both successful recording from large numbers of neurons, six motor nerve recordings and activation of distinct motor behaviors was acquired. Summary of the parameters is shown in table S1. The electrode depths are indicated with respect to the ventral side, which puts the electrode arrays in Rexed laminae VII-VIII, where the motor-related inter-neurons are located.

Rotational dynamics

To substantiate the observation of rotational population dynamics (Fig. 1), we analysed several trials ($n=8$) of the same animal in similar manner (Fig. S1A). The population activity had similar sequential activity. The sorting and PCs are the same as in Fig. 1 and based on trial 3 (indicated by "*"). The distribution of phases, which was calculated with respect to the rhythmic activity of a motor nerve (hip flexor), revealed no clear phase-preference (Fig S1B). The population activity in PCA space indicates similar rotational dynamics (Fig S1C). Analysing all animals in the same manner yielded similar results: Sequential activity in the neuronal population with a continuous cycling through all phases (Fig S2A). Hence, most of the phases were represented and there was no distinct mode to see in the histograms (Fig S2B). The trajectory in PCA space also had resemblance to rotation in other animals (Fig S2C). The dynamics was generally low-dimensional, as manifested by much of the variance is represented by few principal components (Fig S2D).

Activity of excitatory and inhibitory neurons in the BSG-model

The Balanced Sequence Generator (BSG) model introduced in Fig. 2, and described above, exhibits rotational dynamics, in accord with experimental observations. Here, we can further ask what the respective roles of the inhibitory and excitatory populations are during this rotation. In the traditional half-center model, excitatory (E) and inhibitory (I) populations should alternative in activity due to reciprocal connections. In the BSG-model the behavior of the E/I populations are different. Activating the BSG-model with a descending drive causes the neurons to oscillate

(Fig. S3A-B), as seen in Fig. 2. Segregating the population into the E and I and performing the same type of sorting according to phase, there was a similar sequential activity within the E- and I- populations (Fig. S3C-E). Therefore, looking at these populations individually, they also demonstrate rotational dynamics (not shown). This can be considered an experimental prediction of the BSG-model, that make it distinguishable from the half-center model. Another way of showing these properties is by plotting what is called the eigenmode of the network activity (Fig. S3F). Here, each dot represent the activity of a given neuron, in terms of its phase, as the angle in the polar plot, and its firing rate as the radius in the polar plot. The activity is scattered around the origin with many different angles and radii. The different angles indicates that there is no particular phase preference within the population. Similar way of plotting the population activity have been applied in previous reports [15, 16]. Segregating the eigenmode into the E- and I-populations, show similar patterns (Fig. S3G-H). Histograms of the phase of the activity across the neuronal population did illustrate wide phase distribution (Fig. S3I-K). This should be compared with the experimental observed phase distributions (Figs. S1B and S2B.)

Control of force by descending input via the radius of rotation

In figure 2J-P the issue of control of muscular force, i.e. amplitude modulation of the rhythmic nerve output, was considered both in the BSG-model and in experiments. In the BSG-model the control of amplitude was accomplished by modulating the general drive or neuronal gain. When an increase in drive or gain was provided to the whole network, the dynamics of the network becomes slightly more unstable. This was seen as an expansion of the eigenvalue spectrum of the connectivity matrix, W (Fig. S4A). When some of the eigenvalues crossed the stability line (red vertical line) the network starts to oscillate. Sorting the neurons according to phase, a sequential activity was revealed (same sorting throughout, Fig. S4B). As the drive increased, the amplitude also increased. This was also seen in the PCA where the radius of rotation expanding increasing (Fig. S4C). Some of the neurons projected to motor neurons resulting in flexor and extensor ENG activity that also increased in amplitude (Fig. S4D). Note that this control of force did not seem to affect the period of oscillation. This is an advantage of the BSG-model, since other models have not been able to secure independent control of period and amplitude. The correlation between drive, firing rates, nerve output and rotation radius is shown in (Fig. S4E-H). In the experiments, we observed trials that had different radius of rotation (Fig. S1C) that was correlated with the ENG amplitude (Fig. 2N-P). This was further analysed by dividing each trial up in smaller pieces and comparing the PCA rotation and nerve activity (Fig. S5A-F). The nerve output (RMS) had a significant correlation with the radius of PCA rotation both in the presented animal (Fig. S5G) and across all 5 animals (Fig. S5H).

Mean and variance of population activity: BSG- model and experiment

In the above we learned that, when the descending input provide activation of the network, the neurons starts to oscillate. The descending drive can come from many sources, and in the present experiments the source is cutaneous sensory input that elicit a scratching response. Besides starting the rhythmic activity, the variance in activity is also increase, in both the BSG-model and in the experiment (Fig. S6). The variance tend to be larger than the excursions in mean firing rate itself.

Multifunctionalism in the BSG-model and experiment

In figure 4, we observed that both the BSG-model as well as the sampled neuronal population in the experiment, was able to participate and generate two distinct motor behaviors, the pocket- and rostral scratching). Multifunctional circuitry in the spinal cord is well-established [8, 17, 18], but the mechanisms of how a network accomplishes this is an open question. The same BSG-network was able to generate these two patterns by activation of selected subset of neurons that could shift the phase of one output motor nerve (hip extensor), thus providing two distinct motor programs, pocket- and rostral scratching. The BSG-network was in fact able to generate many distinct motor patterns, depending on what subset of neurons that is activated by descending drive. Here, we should a samples of the diversity in motor output by randomly selecting subsets of neurons (Fig. S7A). This resulted in similar albeit not identical sequential activities (Fig. S7B), and rotational population dynamics (Fig. S7C). The resulting motor nerve output of 4 nerves had various and different patterns (Fig. S7D). To compare this with the experimental observation we first look at two trials of same behavior, and then show a trial of another behavior below for four representative animals (Fig. S8). The population activity had a more clear and repeatable sequence, when the animal was repeating the same motor output, compared with a

different motor behavior. Nevertheless, there was similarity in the sequence of patterns despite the difference in motor programs.

Other observations: Non-resetting deletions

A deletion is defined as a brief spontaneous failure of appearance of either a flexor or extensor burst in an otherwise normal robust alternating activity [19, 20]. If the sequence of the rhythm starts over after the deletion, it is referred to as a ‘resetting deletion’. However, if the rhythm as a whole continue uninterrupted, the deletion is referred to as a ‘non-resetting deletion’. The appearance of non-resetting deletions is generally considered evidence for a multi-layered organization within central pattern generators. Here, we observed the phenomenon of non-resetting deletions in a subset of trials (n=2) (Fig. S9). The appearance of such phenomenon is in line with previous observation in this preparation [20], and it suggest to support the notion of multiple layers. Nevertheless, the neuronal population dynamics did not seem particularly affected by the deletion, which suggests that if there is multiple layers, the deletion occurs in a rather small layer or a layer located elsewhere in the spinal cord.

Table S1. Overview of data. Units column represents the number of neurons (units) that was isolated using polytrode spike sorting. Number of trials within each behavior (ipsilateral or contralateral pocket scratching or rostral scratching). The vertebral location indicate where the Berg64-electrode probes were inserted. The VD (ventrodorsal) depth indicated how deep the probes were inserted from the ventral side (preparation was upside-down).

Data set	Units	Behaviors	Trials (ipsi-,contra-pocket, rostral)	Vertebral location	VD-Depth (μm)
1	226	3	14 (6/6/2)	D8, D9, D10	560, 560, 750
2	249	3	10 (4/3/3)	D8, D9, D10	1050, 1235, 1050
3	214	2	19 (10/9/0)	D8, D9, D10	702, 694, 725
4	58	3	16 (5/5/6)	D8, D9, D10	1050, 1060, 1500
5	200	3	23 (6/6/11)	D8, D9 (contralateral), D10	400, 400, 400

4. MATHEMATICAL NOTE ON OSCILLATIONS IN LINEAR DYNAMICAL SYSTEM

In general the activity of a set of variables of a dynamical system can be described by a system of ordinary differential equations where a parallel strings of data points written in compact notation as \mathbf{x} in a dynamical equation:

$$\frac{d}{dt}\mathbf{x}(t) = f(\mathbf{x}) \quad (\text{S13})$$

where function f describes both network interactions as well as intrinsic properties of the neurons in the network.

Let us start with a simple network model where $\mathbf{x}(t)$ represents a vector containing the firing rates (relative to a baseline) of N leaky neurons that are synaptically coupled by a connection matrix \mathbf{W} :

$$\tau \frac{d}{dt}\mathbf{x}(t) = -\mathbf{x} + g\mathbf{W}\mathbf{x} \quad (\text{S14})$$

Here τ is the membrane time constant and g is the slope (gain) of the firing rate function that we assume is linear. This network has an equilibrium point, i.e. a point where $\frac{d}{dt}\mathbf{x}(t) = 0$, at $\mathbf{x}(t) = 0$, corresponding to state in which all neurons fire at the baseline rate. After rewriting Eq.S14 slightly to

$$\frac{d}{dt}\mathbf{x}(t) = \frac{1}{\tau}[g\mathbf{W} - \mathbf{I}] \cdot \mathbf{x} \quad (\text{S15})$$

and defining $\mathbf{A} = \frac{1}{\tau}[g\mathbf{W} - \mathbf{I}]$ we see that our network has the general form of a linear dynamical system

$$\frac{d}{dt}\mathbf{x}(t) = \mathbf{A} \cdot \mathbf{x} \quad (\text{S16})$$

If an input (perturbation) to the network at $t = 0$ is in the direction of one of the eigenvectors \mathbf{r}_k of \mathbf{A} (i.e. population vectors for which $\mathbf{A}\mathbf{r}_k = \lambda_k\mathbf{r}_k$, where λ_k is the corresponding eigenvalue)

the dynamics is given by $\frac{d}{dt}\mathbf{x}(t) = \mathbf{A} \cdot \mathbf{r}_k = \lambda_k \mathbf{r}_k$, which has the solution

$$\mathbf{x}(t) = \mathbf{r}_k e^{\lambda_k t} \quad (\text{S17})$$

Since any perturbation can be expressed as a sum of eigenvectors the stability of the equilibrium point is therefore determined by the distribution of eigenvalues λ_k of the matrix \mathbf{A} .

If all eigenvalues have a real part smaller than zero the activity $\mathbf{x}(t)$ decays back to the equilibrium. In contrast, if at least one eigenvalue has a real part greater than zero the activity of the network is unstable and will grow exponentially due to Eq.S17. The crucial parameter for the stability of the network is thus the largest real part of all the eigenvalues: $\Lambda = \max_k \text{Re}(\lambda_k)$.

Let us next assume that the connectivity matrix \mathbf{W} of our simple network model is balanced, i.e. that excitatory and inhibitory inputs are equally strong for every neuron in the network. Then the eigenvalues spectrum of the static connectivity matrix \mathbf{W} is distributed on a disc in the complex plane centered at zero with a spectral radius determined by the variance of the connectivity [14].

To further analyze our simple network model it is of interest to find the eigenvalues of the matrix $\mathbf{A} = \frac{1}{\tau}[g\mathbf{W} - \mathbf{I}]$. Since the subtraction by the identity matrix \mathbf{I} only shifts the eigenvalue spectrum by -1, the stability criterion outlined above for the largest eigenvalue of \mathbf{A} is equivalent when the largest eigenvalue of the effective connectivity $\mathbf{W}_{\text{eff}} = g\mathbf{W}$ has a real part that crosses 1. Adjusting the gain g of the firing rate function adjusts the spectral radius of \mathbf{W}_{eff} so that the gain can be used as a parameter to adjust the stability of the network.

The eigenvalues of a specific realization of \mathbf{W} may result either in a scenario where the imaginary part of λ_{max} is either zero or non-zero. If the imaginary part is non-zero the solution to Eq.S17 is oscillatory while if the imaginary part is zero the solution is static.

5. SUPPLEMENTARY VIDEOS

Movie S1: PCA rotation. Movie S2: Multifunctionalism limb movement model.

REFERENCES

1. P. C. Petersen and R. W. Berg, "Lognormal firing rate distribution reveals prominent fluctuation-driven regime in spinal motor networks," *eLife* **5**, e18805 (2016).
2. P. C. Petersen and R. W. Berg, "Spinal Cord Preparation from Adult Red-Eared Turtles for Electrophysiological Recordings during Motor Activity," *Bio-protocol* **7**, e2381 (2017).
3. R. W. Berg, "The turtle as a model for spinal motor circuits," in *The Neural Control of Movement*, (Elsevier, 2020), pp. 205–219.
4. M. Radosevic, A. Willumsen, P. C. Petersen, H. Lindén, M. Vestergaard, and R. W. Berg, "Decoupling of timescales reveals sparse convergent CPG network in the adult spinal cord," *Nat. Commun.* **10**, 2937 (2019).
5. S. Walloe, U. V. Nissen, R. W. Berg, J. Hounsgaard, and B. Pakkenberg, "Stereological estimate of the total number of neurons in spinal segment D9 of the red-eared turtle." *J. Neurosci.* **31**, 2431–2435 (2011).
6. B. A. Bannatyne, Z.-Z. Hao, G. M. C. Dyer, M. Watanabe, D. J. Maxwell, and A. Berkowitz, "Neurotransmitters and Motoneuron Contacts of Multifunctional and Behaviorally Specialized Turtle Spinal Cord Interneurons," *The J. Neurosci.* **40** (2020).
7. P. S. G. Stein, "Central pattern generators in the turtle spinal cord: selection among the forms of motor behaviors," *J. Neurophysiol.* **119**, 422–440 (2018).
8. A. Berkowitz, A. Roberts, and S. R. Soffe, "Roles for multifunctional and specialized spinal interneurons during motor pattern generation in tadpoles, zebrafish larvae, and turtles," *Front. Behav. Neurosci.* **4** (2010).
9. S. N. Kadir, D. F. M. Goodman, and K. D. Harris, "High-dimensional cluster analysis with the masked EM algorithm." *Neural Comput.* **26**, 2379–94 (2014).
10. R. W. Berg, D. Whitmer, and D. Kleinfeld, "Exploratory whisking by rat is not phase locked to the hippocampal theta rhythm." *J. Neurosci.* **26**, 6518–22 (2006).
11. D. Percival and A. Walden, *Spectral analysis for physical applications - Multitaper and conventional univariate techniques* (Cambridge: Cambridge University Press., 1998).
12. K. V. Mardia and P. E. Jupp, *Directional Statistics* (Wiley and sons, Chichester, 2000).
13. J. P. Stroud, M. A. Porter, G. Hennequin, and T. P. Vogels, "Motor primitives in space and time via targeted gain modulation in cortical networks," *Nat. Neurosci.* **21**, 1774–1783 (2018).
14. K. Rajan and L. F. Abbott, "Eigenvalue spectra of random matrices for neural networks," *Phys. Rev. Lett.* **97** (2006).

15. A. C. Kwan, S. B. Dietz, G. Zhong, R. M. Harris-Warrick, and W. W. Webb, "Spatiotemporal dynamics of rhythmic spinal interneurons measured with two-photon calcium imaging and coherence analysis." *J Neurophysiol* **104**, 3323–3333 (2010).
16. T. A. Machado, "Probing circuits for spinal motor control," Ph.D. thesis, Columbia University Academic Commons (2015).
17. A. Berkowitz, "Multifunctional and specialized spinal interneurons for turtle limb movements." *Annals New York Acad. Sci.* **1198**, 119–132 (2010).
18. A. Berkowitz and Z.-Z. Hao, "Partly Shared Spinal Cord Networks for Locomotion and Scratching." *Integr. comparative biology* pp. 1–13 (2011).
19. G. Zhong, N. A. Shevtsova, I. A. Rybak, and R. M. Harris-Warrick, "Neuronal activity in the isolated mouse spinal cord during spontaneous deletions in fictive locomotion: insights into locomotor central pattern generator organization," *The J. Physiol.* **590** (2012).
20. P. S. G. Stein and S. Daniels-McQueen, "Modular organization of turtle spinal interneurons during normal and deletion fictive rostral scratching." *J. Neurosci.* **22**, 6800–6809 (2002).

LIST OF FIGURES

S1	Rotational population dynamics across trials in the lumbar spinal motor network during rhythmic movement. (A) The firing rates (normalized, color coded) of 214 spinal neurons in laminae VII-VIII as a function of time and sorted according to phase with respect to the nerve activity (hip flexor). Eight consecutive trials from same experiment with a 5 min pause in between each. (B) The phase distribution across the neuronal population. (C) The population activity has rotational dynamics, as demonstrated by the circular motion of the first two principal components. The PCs were calculated by the data of one trial (trial 3, "*") and the applied to the rest of the trials. Bottom scale bars represent 1000.	12
S2	Rotational population dynamics in a spinal motor networks across animals. (A) The rhythmic firing rates in populations of spinal neurons in laminae VII-VIII shown in colors as a function of time and sorted according to phase with respect to a nerve (hip flexor). A representative trial from 5 experiments of approximately 10 seconds demonstrate similar sequential/rotational population activity. Animal used in Fig. S1 is marked "*". (B) The corresponding distribution of neurons having preferred phases among the population of rhythmic neurons. (C) Population activity represented by first two principal components exhibit rotational dynamics. Scale bars: 250. (D) Cumulative explained variance by principal components, indicating the population dynamics is low-dimensional, i.e. most of the variance is captured by few components.	13
S3	Rotational ensemble activity within the excitatory and inhibitory sub-populations in the BSG-model. (A). Activation of the motor circuit by descending drive. (B) The firing rates of 10 sample excitatory neurons as a consequence of the descending input. (C) Sorting the excitatory neurons according to phase of firing rates reveals a sequential activity similar to the previously observed for all neurons. (D-E) Activity and similar sorting of the inhibitory sub-populations reveals similar sequential and rotational dynamics within that sub-population. (F) The network eigenmode for the whole network: Each dot represent both the phase (the polar angle) and the peak firing rate (the radius) for a given neuron ($n=200$). (G-H) Similar plot for the excitatory and inhibitory populations (I-K) the distribution of phases in linear histograms for all neurons (I), excitatory (J) and inhibitory neurons (K). To be compared with experimental distributions (Figs. S1B and S2B).	14
S4	BSG-model: Correlation between descending drive and radius of rotation as well as amplitude of nerve output without affecting the period. (A) For low descending drive and neuronal gain (top), the eigenvalue spectrum does not have any eigenvalues that cross the stability line (broken vertical line). As the drive increases (downward direction) the spectrum expands and eigenvalues cross the stability line. For larger drive the eigenvalues cross the stability line farther. (B) The associated population dynamics (sorted firing rates) exhibit oscillation of increasing magnitude as the drive increase. (C) The rotational dynamics also has a radius that increases with increasing drive. (D) The resulting motor nerve output is also increasing in amplitude. (E) Descending drive (gain) versus the population firing rate (RMS), radius of rotation in PC space (F) and amplitude of nerve output (flexor RMS) (G). The radius of rotation (PC1 RMS) vs. the nerve amplitude (flexor RMS).	15
S5	Radius of rotation correlates with nerve output in experiment. (A) Sample trial where the population activity was divided up in pieces with the corresponding nerve output (B). (C) The PC manifolds had rotation with varying radius. (D-F) other pieces with same organization. (G) The RMS of the nerve activity versus the RMS of the two first principal components for various pieces of activity had a significant correlation. (H) The R^2 values for all animal tested ($n=5$). *: F-statistic of rejection of no trend at $p < 0.01$. (F) Scale bar: 1000.	16
S6	Variance of population firing rate increase during network output: model and experiment. (Aa) The flexor/extensor nerve output from the BSG-network. (b) The sorted neuronal population firing rate ($n=400$ neurons) with rotational dynamics. (c) Color map of the population firing rate. (d) Mean (red) and variance of the population activity. (B) Same organization as in (A), but for experimental data. Animal no. 3 trial 8.	17

S7	Multifunctionalism in the BSG-model. (A) Five examples of specific activation/modulation of selected neurons in the network ("activation profiles"). The top profile has a an even distribution, whereas all the below profiles has selective modulation of specific neurons. (B) The ensemble activity as a result of the activation profile show a sequential activity, with similar but not identical sequence of activity. (C) The first two principal components, based on the top activation profile, all exhibit rotational dynamics, albeit with different radius and trajectories. (D) the output motor patterns associated with the different activation profiles and ensemble activities.	18
S8	Resemblance of sequential network activity across trials and distinct motor behaviors. (A) Experiment 1: (Top) First trial of a motor behavior (pocket hindlimb scratching) with the rhythmic firing rates in populations of spinal neurons shown in colors as a function of time and sorted according to phase, with the 6 motor nerves below to indicate the motor behavior. (Middle): Second trial, and same behavior as shown in top traces. (Bottom): A different motor behavior (rostral hindlimb scratching). (B-D) Same as in A but the different experiments.	19
S9	Two instances of non-resetting deletions. (A) First trial of a motor behavior (pocket hindlimb scratching) with the rhythmic firing rates in populations of spinal neurons shown in colors as a function of time and sorted according to phase, with the 6 motor nerves below to indicate the motor behavior. A deletion is observed in the hip extensor nerve recording (red arrow) whereas the hip flexor (bottom trace) seems to continue and combine two cycles although with a small decrease. (B) Another trial of same behavior with a deletion occurring at similar time point (red arrow). Again, the population dynamics seems unaffected by the deletion. . .	20

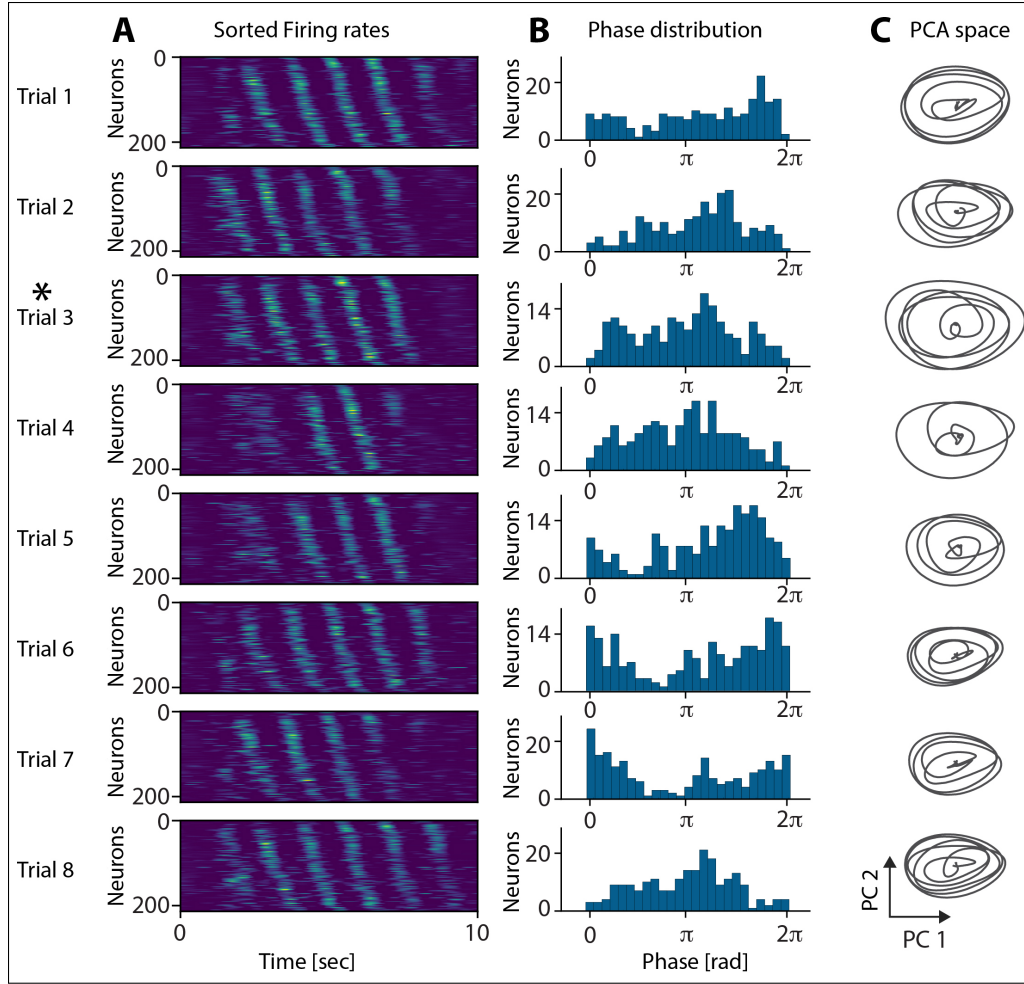


Fig. S1. Rotational population dynamics across trials in the lumbar spinal motor network during rhythmic movement. (A) The firing rates (normalized, color coded) of 214 spinal neurons in laminae VII-VIII as a function of time and sorted according to phase with respect to the nerve activity (hip flexor). Eight consecutive trials from same experiment with a 5 min pause in between each. (B) The phase distribution across the neuronal population. (C) The population activity has rotational dynamics, as demonstrated by the circular motion of the first two principal components. The PCs were calculated by the data of one trial (trial 3, "*") and the applied to the rest of the trials. Bottom scale bars represent 1000.

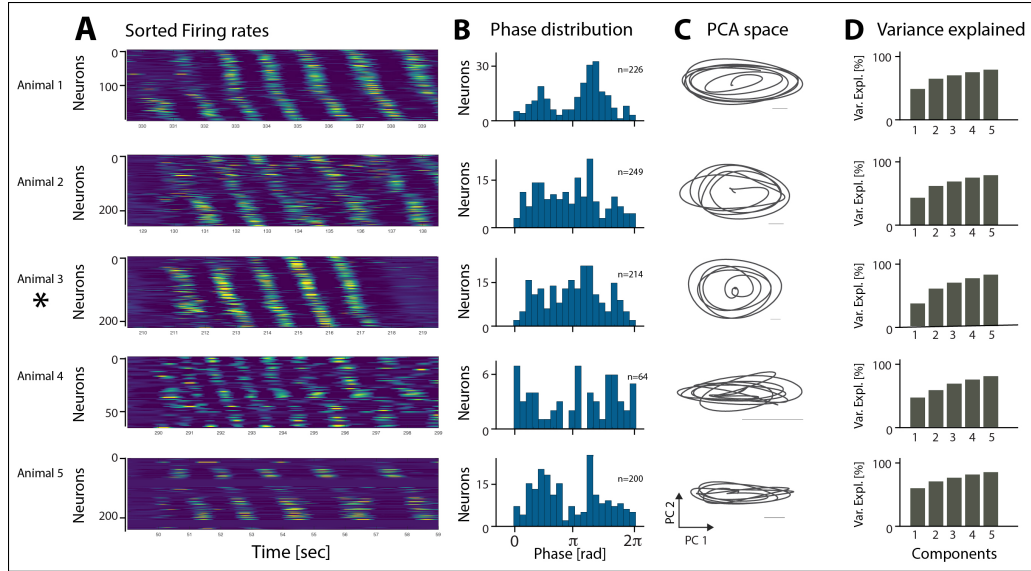


Fig. S2. Rotational population dynamics in a spinal motor networks across animals. (A) The rhythmic firing rates in populations of spinal neurons in laminae VII-VIII shown in colors as a function of time and sorted according to phase with respect to a nerve (hip flexor). A representative trial from 5 experiments of approximately 10 seconds demonstrate similar sequential/rotational population activity. Animal used in Fig. S1 is marked "*". (B) The corresponding distribution of neurons having preferred phases among the population of rhythmic neurons. (C) Population activity represented by first two principal components exhibit rotational dynamics. Scale bars: 250. (D) Cumulative explained variance by principal components, indicating the population dynamics is low-dimensional, i.e. most of the variance is captured by few components.

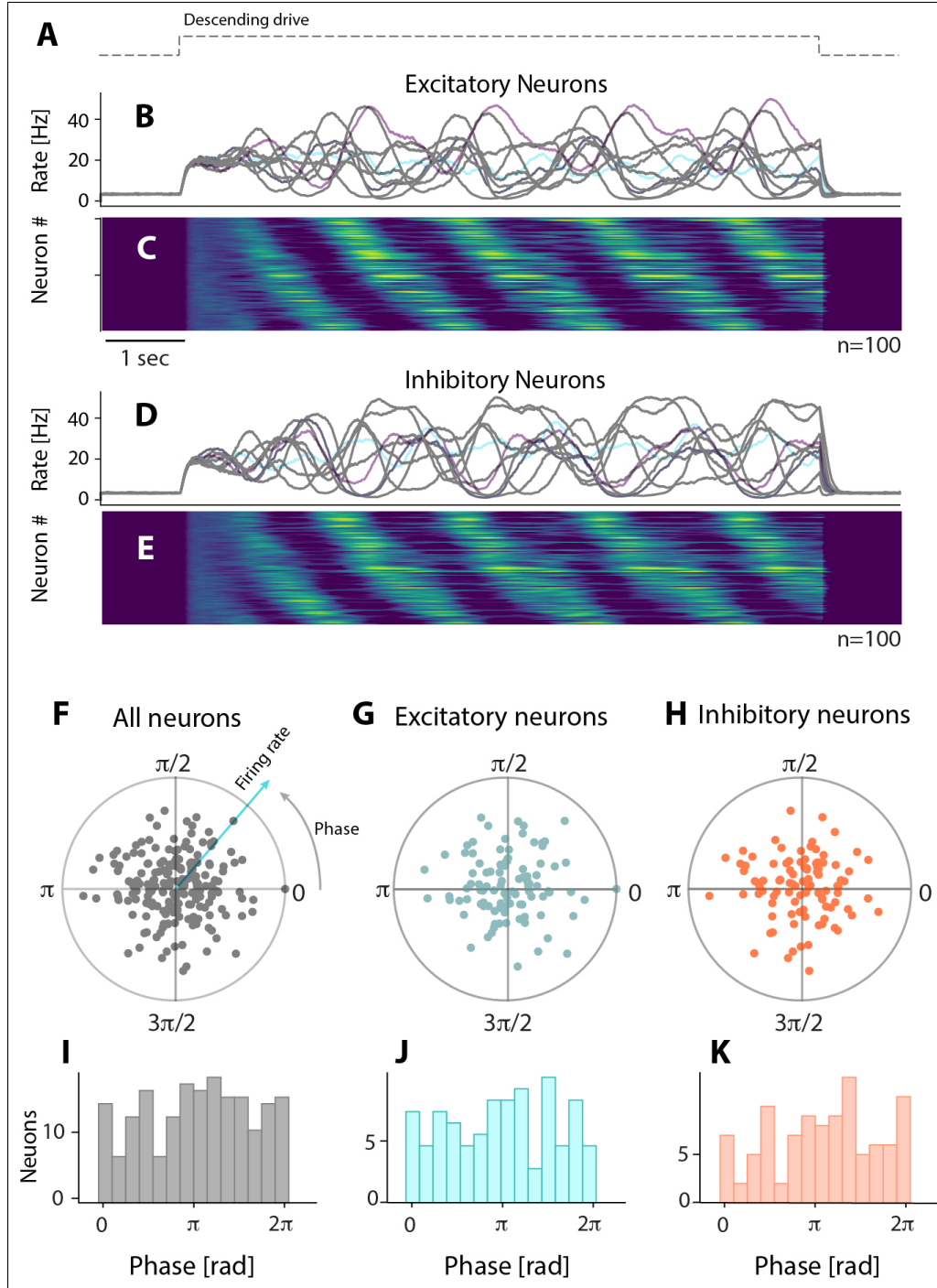


Fig. S3. Rotational ensemble activity within the excitatory and inhibitory sub-populations in the BSG-model. (A). Activation of the motor circuit by descending drive. (B) The firing rates of 10 sample excitatory neurons as a consequence of the descending input. (C) Sorting the excitatory neurons according to phase of firing rates reveals a sequential activity similar to the previously observed for all neurons. (D-E) Activity and similar sorting of the inhibitory sub-populations reveals similar sequential and rotational dynamics within that sub-population. (F) The network eigenmode for the whole network: Each dot represent both the phase (the polar angle) and the peak firing rate (the radius) for a given neuron ($n=200$). (G-H) Similar plot for the excitatory and inhibitory populations (I-K) the distribution of phases in linear histograms for all neurons (I), excitatory (J) and inhibitory neurons (K). To be compared with experimental distributions (Figs. S1B and S2B).

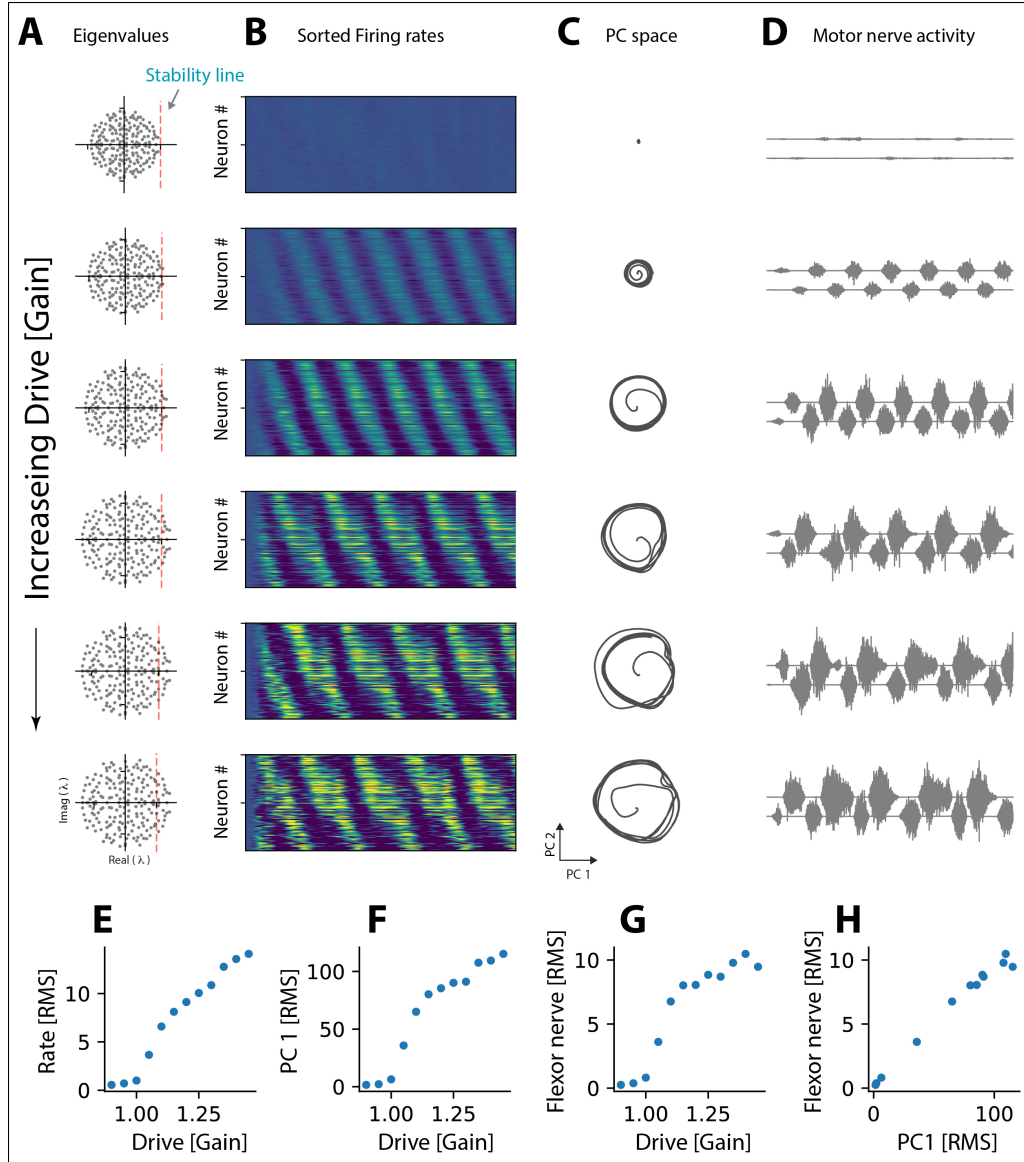


Fig. S4. BSG-model: Correlation between descending drive and radius of rotation as well as amplitude of nerve output without affecting the period. (A) For low descending drive and neuronal gain (top), the eigenvalue spectrum does not have any eigenvalues that cross the stability line (broken vertical line). As the drive increases (downward direction) the spectrum expands and eigenvalues cross the stability line. For larger drive the eigenvalues cross the stability line farther. (B) The associated population dynamics (sorted firing rates) exhibit oscillation of increasing magnitude as the drive increase. (C) The rotational dynamics also has a radius that increases with increasing drive. (D) The resulting motor nerve output is also increasing in amplitude. (E) Descending drive (gain) versus the population firing rate (RMS), radius of rotation in PC space (F) and amplitude of nerve output (flexor RMS) (G). The radius of rotation (PC1 RMS) vs. the nerve amplitude (flexor RMS).

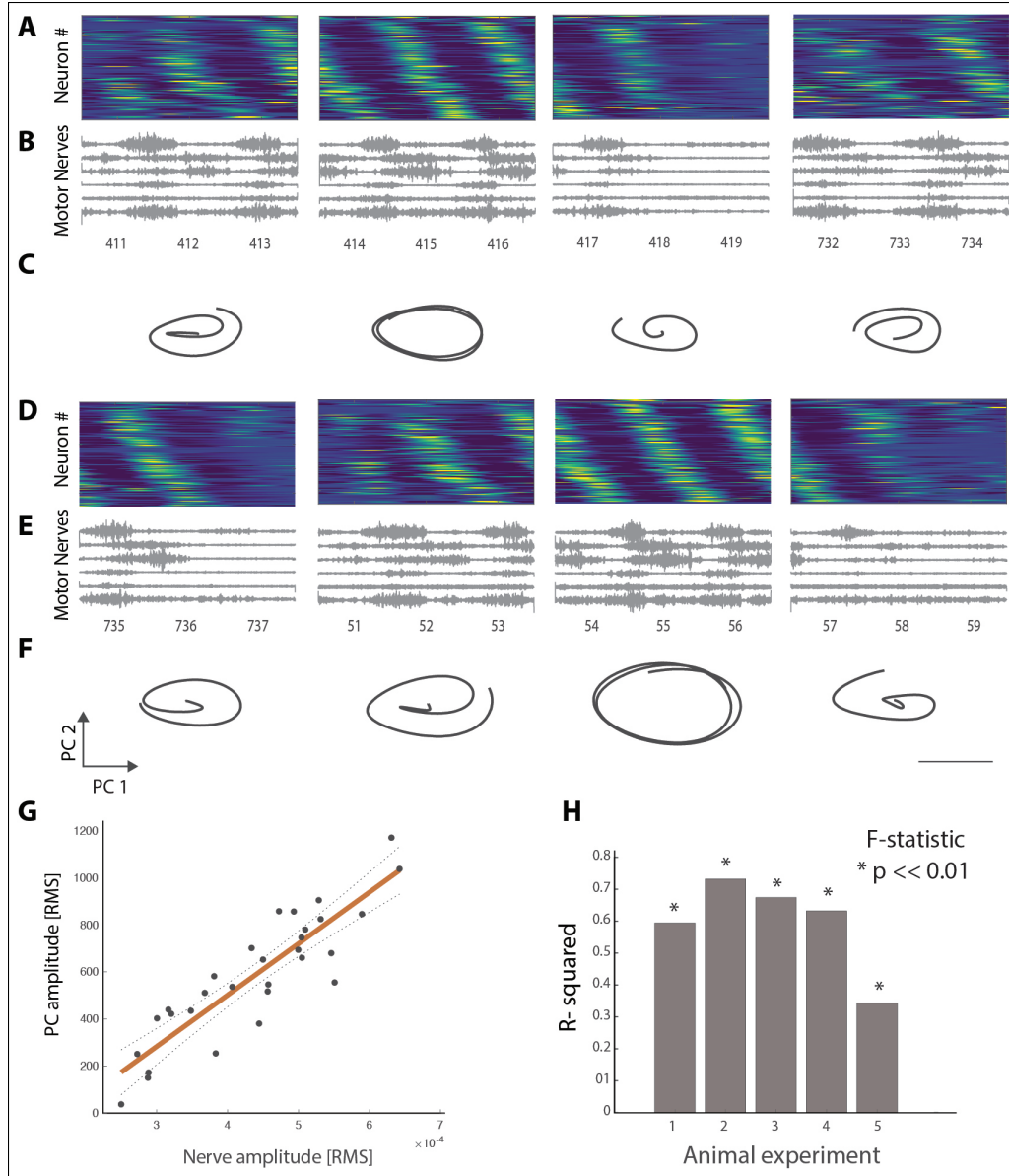


Fig. S5. Radius of rotation correlates with nerve output in experiment. (A) Sample trial where the population activity was divided up in pieces with the corresponding nerve output (B). (C) The PC manifolds had rotation with varying radius. (D-F) other pieces with same organization. (G) The RMS of the nerve activity versus the RMS of the two first principal components for various pieces of activity had a significant correlation. (H) The R^2 values for all animal tested ($n=5$). *: F-statistic of rejection of no trend at $p < 0.01$. (F) Scale bar: 1000.

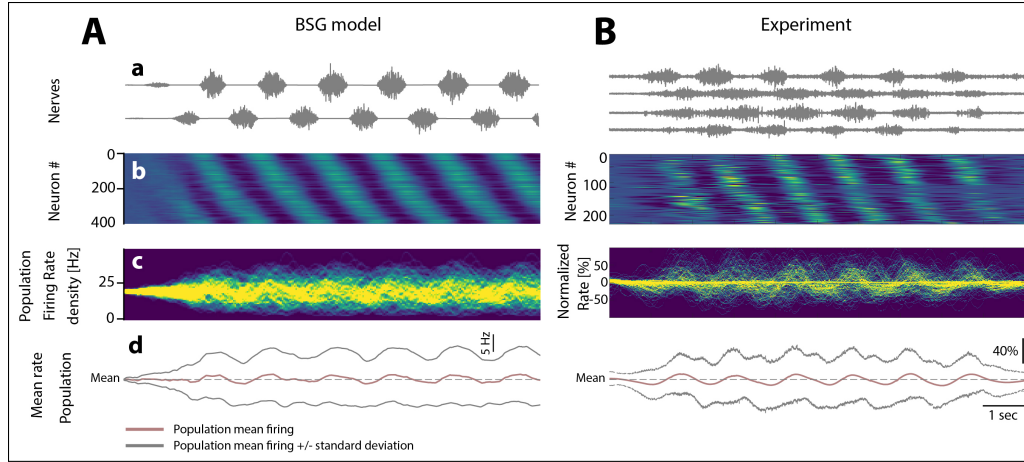


Fig. S6. Variance of population firing rate increase during network output: model and experiment. (Aa) The flexor/extensor nerve output from the BSG-network. (b) The sorted neuronal population firing rate (n=400 neurons) with rotational dynamics. (c) Color map of the population firing rate. (d) Mean (red) and variance of the population activity. (B) Same organization as in (A), but for experimental data. Animal no. 3 trial 8.

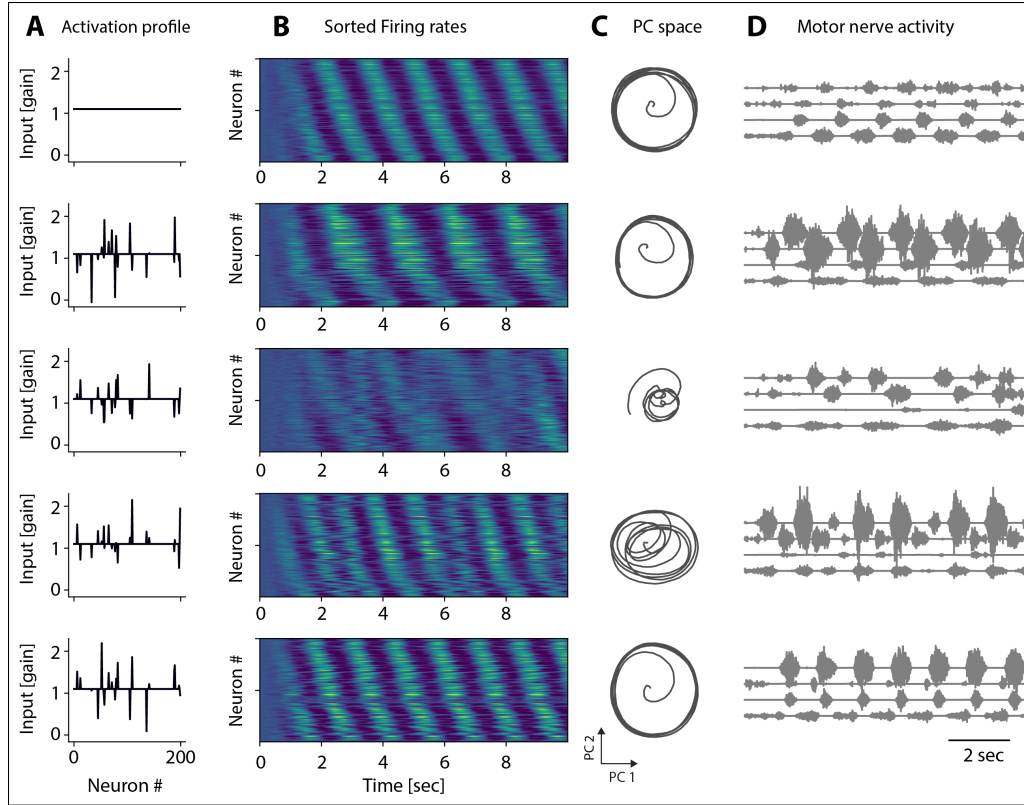


Fig. S7. Multifunctionalism in the BSG-model. (A) Five examples of specific activation/modulation of selected neurons in the network ("activation profiles"). The top profile has a an even distribution, whereas all the below profiles has selective modulation of specific neurons. (B) The ensemble activity as a result of the activation profile show a sequential activity, with similar but not identical sequence of activity. (C) The first two principal components, based on the top activation profile, all exhibit rotational dynamics, albeit with different radius and trajectories. (D) the output motor patterns associated with the different activation profiles and ensemble activities.

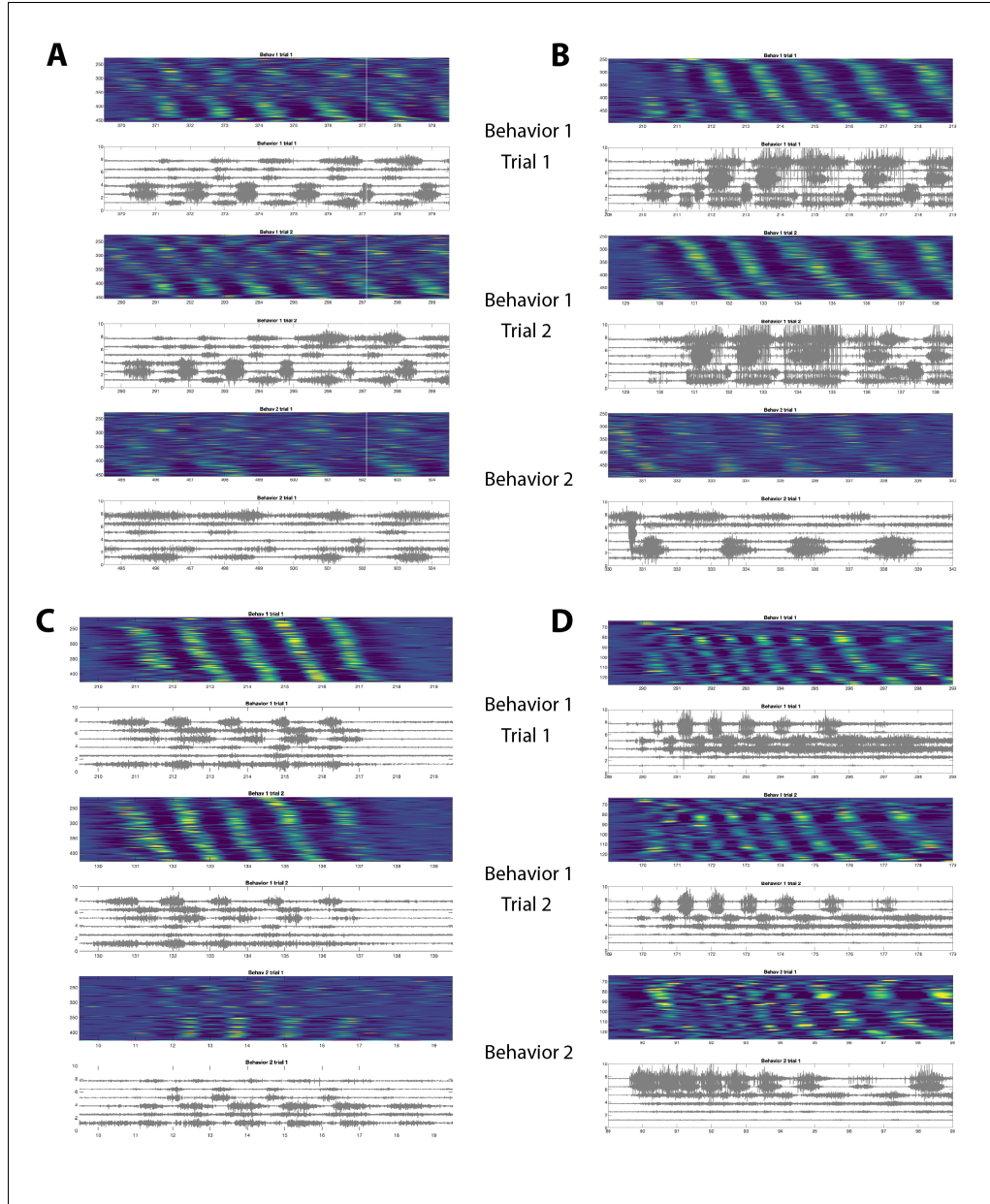


Fig. S8. Resemblance of sequential network activity across trials and distinct motor behaviors. (A) Experiment 1: (Top) First trial of a motor behavior (pocket hindlimb scratching) with the rhythmic firing rates in populations of spinal neurons shown in colors as a function of time and sorted according to phase, with the 6 motor nerves below to indicate the motor behavior. (Middle): Second trial, and same behavior as shown in top traces. (Bottom): A different motor behavior (rostral hindlimb scratching). (B-D) Same as in A but the different experiments.

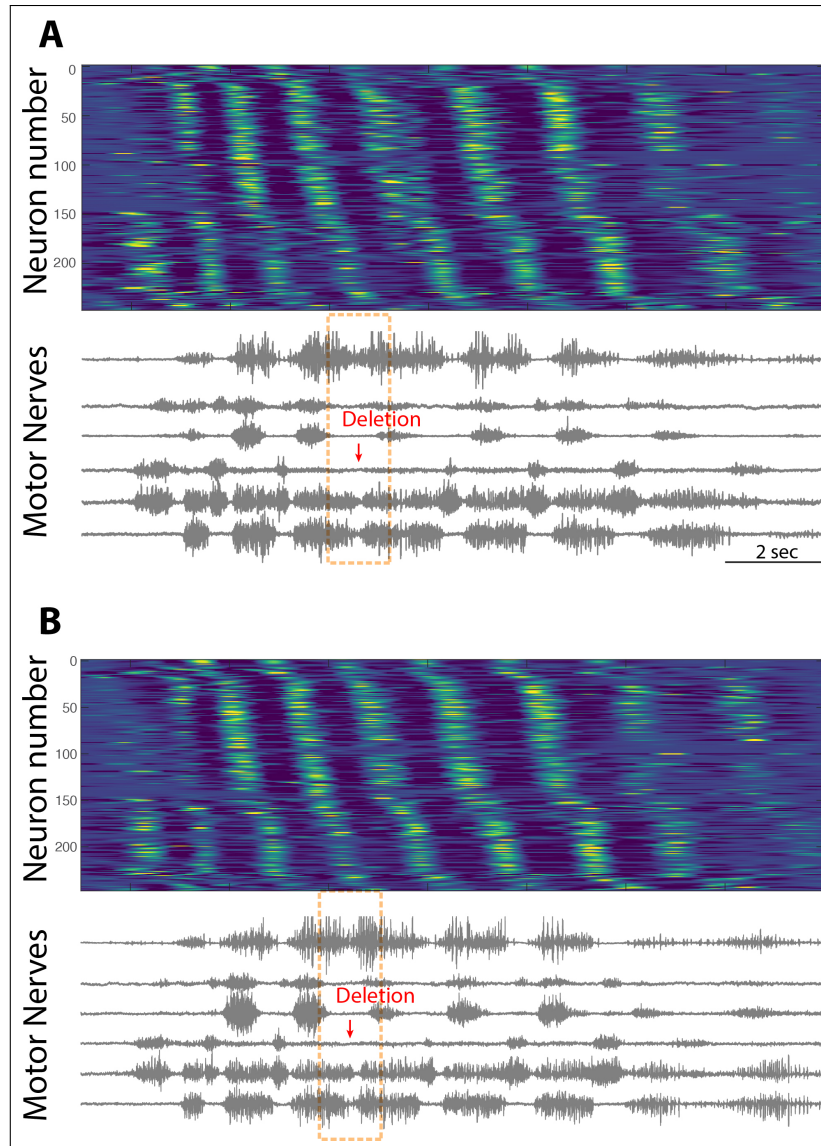


Fig. S9. Two instances of non-resetting deletions. (A) First trial of a motor behavior (pocket hindlimb scratching) with the rhythmic firing rates in populations of spinal neurons shown in colors as a function of time and sorted according to phase, with the 6 motor nerves below to indicate the motor behavior. A deletion is observed in the hip extensor nerve recording (red arrow) whereas the hip flexor (bottom trace) seems to continue and combine two cycles although with a small decrease. **(B)** Another trial of same behavior with a deletion occurring at similar time point (red arrow). Again, the population dynamics seems unaffected by the deletion.